Free-induction-decay magnetometer for pulsed eddy current testing

Zixuan Xiao, Kaiwen Yi, Zejia Lin, and Xiang Peng[*]
School of Electronics, Peking University, Beijing 100871, China

(Received 15 December 2025; accepted 20 April 2026; published 18 May 2026)

Pulsed-eddy-current testing (PECT) is a highly efficient active detection technique used in nondestructive testing of conductive structures, transient electromagnetic exploration for mineral resources, and the detection of unexploded ordnance. To directly measure the induced magnetic field and improve the sensitivity of PECT systems, we use a free-induction-decay (FID) atomic magnetometer instead of pickup coils, enabling improved detection of weak low-frequency signals. The FID magnetometer employs an enhanced-optical-pumping scheme and an instantaneous phase-retrieval method, achieving a noise floor of 0.45 pT/$\sqrt{\mathrm{Hz}}$ and bandwidth of 4.2 kHz. The synchronized magnetic-pulse pumping scheme not only significantly amplifies the spin polarization of the atomic ensemble to strengthen the FID signal and improve sensitivity, but also induces eddy-current magnetic fields in nearby metallic conductors. Using instantaneous phase retrieval, we extract the pulsed-eddy-current magnetic fields from the FID signal and determine their characteristic time constant (τ). The FID magnetometer is validated for measuring pulsed-eddy-current magnetic fields generated by multiple metals, including copper, aluminum, zinc, and lead. This work demonstrates the potential of the FID magnetometer for applications in magnetic induction tomography and remote-field eddy-current testing.

DOI: 10.1103/6j4p-fs75

I. INTRODUCTION

Pulsed-eddy-current testing (PECT) technology has been widely employed in fields such as metallic nondestructive testing [1–3], transient electromagnetic surveys for mineral exploration [4,5], and unexploded ordnance detection [6–8], owing to its advantages of noninvasive nature, rapid transient signal detection capability, and broad detection range. The PECT system operates based on electromagnetic induction, with its working principle illustrated in Fig. 1(a). First, a transmitting coil emits a primary time-varying magnetic field $\mathbf{B}_{\mathrm{p}}$, which induces eddy currents on the surfaces of metallic conductors. These eddy currents in turn produce a decaying secondary magnetic field $\mathbf{B}_{\mathrm{ec}}$, which is then detected by pickup coils. The transient response of the induced voltage is analyzed to characterize the electrical properties of the conductors; however, the sensitivity of pickup coils is fundamentally constrained by their reliance on the temporal derivative of the magnetic field. This poses a significant challenge for detecting weak eddy-current magnetic fields at low frequencies, which in turn constrains the effectiveness of conventional PECT systems [9]. In such scenarios, directly measuring the magnetic field, rather than its rate of change, is more advantageous. Accordingly, magnetic sensors such as Hall sensors [10], giant magnetoresistance sensors [11], and superconducting quantum interference devices [12] have been widely adopted for PECT systems.

With the rapid advancement of quantum sensing technologies, optically pumped magnetometers (OPMs) have seen significant development due to their high sensitivity, wide dynamic range, elimination of the need for cryogenic operation, and potential for miniaturization [13–15]. These highly sensitive devices have been widely applied in areas such as fundamental physics [15,16], space magnetometry [16,17], and biomedical imaging [18–20]. Nevertheless, despite considerable efforts by previous researchers [21], only a limited number of OPMs are suitable for PECT. Since performing PECT requires OPMs to operate stably and reliably under strong alternating magnetic fields, this imposes stringent demands on their dynamic range and slew rate. Radio-frequency magnetometers are the most commonly used OPMs for eddy-current testing (ECT). These devices can detect alternating magnetic fields oscillating at the Larmor frequency under a constant-bias magnetic field and are primarily used for single-frequency ECT [22–24]. Although PECT offers the advantage of clear temporal separation between excitation and eddy-current fields, implementing this technique in atomic magnetometers remains challenging.

Recently, OPMs operating in the free-induction-decay (FID) scheme have attracted significant attention due to their compact structure, small systematic errors, and high robustness [25–28]. Since the atomic spin precession frequency responds instantaneously to changes in the ambient magnetic field [15,29], this enables the detection of transient eddy-current magnetic fields through the measurement of atomic spin precession. Additionally, the temporal separation of pump and probe in FID magnetometers makes them highly promising for PECT.

[*]Contact author: xiangpeng@pku.edu.cn

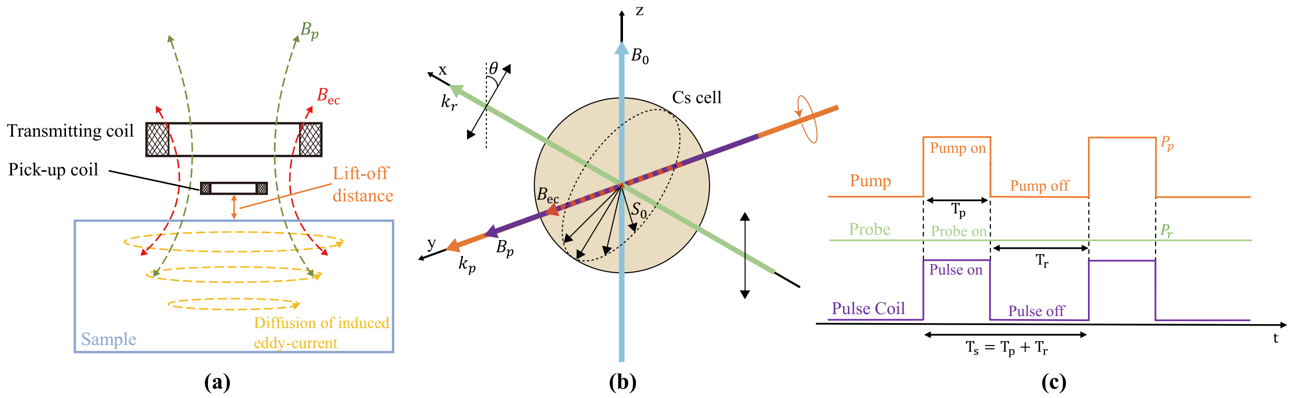

FIG. 1. (a) Schematic illustration of the working principle of the PECT system with pickup coil. Here, the Lift-off distance is the vertical distance between the coil and the metal plate. (b) Geometry of the enhanced-optical-pumping FID magnetometer for PECT. Here, $\mathbf{B}_0$ is the constant-bias magnetic field; $\mathbf{k}_\mathrm{p}$ and $\mathbf{k}_\mathrm{r}$ are the propagation vectors of the circularly polarized pump beam and the linearly polarized probe beam, respectively; $\mathbf{S}_0$ is the initial spin orientation created during the pump stage; θ is the polarization-rotation angle of the probe beam; $\mathbf{B}_\mathrm{p}$ is the pulsed magnetic field generated by the pulsed coil; and $\mathbf{B}_\mathrm{ec}$ is the eddy-current magnetic field induced by the pulsed coil. (c) Timing control sequences of the pump beam, probe beam, pulsed coil, and signal recording. In a single measurement cycle of duration $T_\mathrm{s} = T_\mathrm{p} + T_\mathrm{r}$, spin polarization of cesium (Cs) is generated by the combination of the pump light with peak power P_p and the pulsed magnetic field, both applied for a duration T_p. After the pump light and pulsed magnetic field are switched off simultaneously, the FID signal is read by a weak probe beam with constant power P_r for a duration T_r.

The standard operating procedure of the conventional FID magnetometer is as follows [30–32]: (1) generate appreciable spin polarization via synchronous optical pumping; (2) fit the FID signal to extract a single Larmor precession frequency; and (3) repeat the pump-probe cycle to acquire a sequence of Larmor frequencies. Nonetheless, similar to the averaging-type magnetometers such as Bell-Bloom schemes [33], conventional FID magnetometers remain challenging for PECT, as they provide magnetic field information averaged over the processes of state preparation, evolution, and detection, rather than the instantaneous magnetic field [16]. Moreover, when the external magnetic field changes rapidly, such magnetometers cannot operate reliably [21]. These limitations mainly arise from the pumping scheme and the signal-processing approach. In the synchronous optical pumping scheme, rapidly varying external magnetic fields may cause the system to lose lock and require a finite time to re-establish tracking of the magnetic field and readjust the modulation frequency, during which part of the transient eddy-current magnetic field information may be lost. From the signal-processing perspective, conventional FID magnetometer algorithms output the average magnetic field over a measurement cycle [34]; however, eddy-current magnetic fields in PECT can decay rapidly and vanish within a single cycle, causing such cycle-averaging algorithms to fail to capture the instantaneous variations of transient eddy-current magnetic fields.

In this paper, we propose an alternative approach to PECT by using an FID magnetometer to detect and characterize the pulsed-eddy-current magnetic fields generated by four distinct metals: copper (Cu), aluminum (Al), zinc (Zn), and lead (Pb). To address the limitations of conventional FID magnetometers in PECT, we modify both the pumping scheme and the signal-processing method, specifically adopting an enhanced-optical-pumping scheme and the Hilbert transform. The pumping scheme uses an intense pulsed magnetic field for auxiliary pumping, which not only significantly improves the polarization of the atomic ensemble to amplify the FID signal and improve sensitivity, but also induces eddy-current magnetic fields in nearby metallic conductors. This intense pulsed magnetic field serves as the alternating magnetic field in PECT systems, effectively overcoming the challenge of atomic ensembles struggling to achieve high spin polarization under alternating magnetic fields. Furthermore, with this pumping scheme, the FID magnetometer can operate without prior estimation of the magnitude of the ambient magnetic field and without the need for an additional closed-loop feedback circuit. Regarding signal processing, in contrast to conventional FID magnetometers, which output the average magnetic field over a single measurement cycle, our approach extracts the instantaneous variation of the magnetic field within the measurement cycle. By performing the Hilbert transform on the FID signal, we retrieve its instantaneous phase and further derive its instantaneous frequency [35]. This signal-processing method enables the FID magnetometer to achieve a high bandwidth and allows for accurate reconstruction of the temporal evolution of eddy-current magnetic fields.

The remainder of this paper is organized as follows. Section II describes the operating principle and experimental setup of the proposed magnetometer. Section III presents the magnetometer's performance and its measurement results for pulsed-eddy-current magnetic fields. Section IV concludes the work and discusses potential applications of the proposed PECT scheme.

II. OPERATING PRINCIPLE AND EXPERIMENTAL SCHEME

A schematic diagram of PECT using the enhanced-optical-pumping FID magnetometer is shown in Fig. 1(b). A constant-bias magnetic field $\mathbf{B}_0$ is oriented along the z axis. The pump and probe beams are mutually orthogonal in the x–y plane, with the pump light propagating along the y axis. The FID magnetometer operates in two consecutive steps of pumping and probing, with the timing sequence depicted in Fig. 1(c).

During the pumping stage, circularly polarized light is used to generate spin polarization. To facilitate efficient spin polarization buildup of cesium atoms, an additional pulsed magnetic field $\mathbf{B}_p$, generated by the pulsed coil, is applied synchronously with the pump light. This enhanced-optical-pumping approach has been widely adopted in recent magnetometer research and achieves pumping efficiency comparable to synchronous optical pumping [36].

In the probing stage, both the pump light and the pulsed magnetic field are switched off simultaneously. When conductive materials are placed near the pulsed coil, an eddy-current magnetic field $\mathbf{B}_{ec}$ is induced according to electromagnetic induction. This field decays over time and is oriented in the same direction as the pulsed magnetic field $\mathbf{B}_p$. The atomic spins then precess under the combined effect of the bias magnetic field $\mathbf{B}_0$ and the eddy-current magnetic field $\mathbf{B}_{ec}$. The Faraday rotation of a detuned, weak, linearly polarized probe beam is recorded using balanced polarimetry. To extract the instantaneous Larmor frequency of the total magnetic field, an instantaneous phase-extraction method based on the Hilbert transform is applied [35].

The pump-probe cycle, illustrated in Fig. 1(c), has a total duration T_s and consists of two stages: a pumping stage with peak power P_p and duration T_p, followed by a probing stage with constant power P_r and readout time T_r. By optimizing the optical power of the probe light, the transverse relaxation time of the atomic spins can be made longer than the duration of the eddy-current magnetic field, allowing a nearly complete measurement of its temporal evolution.

The dynamics of the spin orientation $\mathbf{S}$ in the FID magnetometer are described by the Bloch equation [25,31],

$$\frac{d\mathbf{S}}{dt} = \gamma \mathbf{S} \times (\mathbf{B}_0 + \mathbf{B}_{ec}) - \Gamma_1 S_z \mathbf{e}_z - \Gamma_2 (S_x \mathbf{e}_x + S_y \mathbf{e}_y), \quad (1)$$

where $\gamma \simeq 2\pi \times 3.5$ Hz/nT is the gyromagnetic ratio of the Cs atomic ground state, $\mathbf{B}_0$ is the constant-bias magnetic field, and $\mathbf{B}_{ec}$ is the eddy-current magnetic field induced by the pulsed excitation. Additionally, Γ_1 and Γ_2 denote the longitudinal and transverse relaxation rates, respectively. We set $\mathbf{B}_0 = B_0 \mathbf{e}_z$ and assume $\Gamma_1 \approx \Gamma_2 = \Gamma$, which is a reasonable approximation for an isotropic medium [37]. The direction of the eddy-current magnetic field can be arbitrary, except within the detection dead zone along the z axis. In the present experimental setup, the eddy-current magnetic field is oriented along the y axis, i.e., $\mathbf{B}_{ec} = B_{ec} \mathbf{e}_y$. Although the eddy-current magnetic field decays over time, it can be reasonably approximated as a static field affecting the atomic spins. Substituting these conditions into Eq. (1) and applying the initial condition $\mathbf{S}(t = 0) = S_0 \mathbf{e}_y$, the component of the orientation polarization along the probe beam direction is

$$S_x(t) = S_0 \sqrt{\frac{B_0^2}{B_0^2 + B_{ec}^2}} e^{-\Gamma t} \sin(\omega_L t), \quad (2)$$

where $\omega_L = \gamma \sqrt{B_0^2 + B_{ec}^2}$ is the Larmor frequency. The optical rotation angle of the linearly polarized probe beam is proportional to the spin polarization S_x [28]. Although this model is simplified, it demonstrates that the eddy-current magnetic field is encoded in the phase of the FID signal.

The experimental setup for PECT is shown in Fig. 2(a). The Cs atoms are contained in a cylindrical vapor cell with a 25 mm diameter and 35 mm length. The walls are antirelaxation coated to extend the coherence between ground-state Zeeman sublevels. To ensure that the FID signal fully captures the decay of the eddy-current magnetic field and allows rapid progression to the next pump-probe cycle, the transverse relaxation time is set to $T_2 = 16$ ms. Optimized buffer gas cells or multipass cells can also be used with this scheme [38–40]. The cell is maintained at room temperature and positioned at the center of a seven-layer μ-metal magnetic shield to suppress technical noise. A constant bias magnetic field $B_0 = 5$ μT is applied along the z axis as a typical experimental value; this can be increased if the magnetic-field gradient does not induce a stronger relaxation effect. This field is generated by a three-axis Helmholtz coil driven by a stable dc current source (Krohn-Hite Model 523). A pulsed magnetic field is generated by a flexible printed circuit board (FPCB) coil with a compact biplanar stack, which can generate stronger magnetic fields than a single-layer FPCB. The coil constant is calibrated using a fluxgate magnetometer, yielding 1 μT/mA at the center of the vapor cell. The pulsed coil is driven by an arbitrary-function generator (Keysight 33500B series), with rapid switch-off achieved by connecting the coils in parallel with a small resistor. The switch-off time, measured with an oscilloscope (Keysight InfiniiVision 2000 X), is 2 μs. The atomic vapor cell, pulsed coil, and metal plate are integrated within a custom 3D-printed acrylonitrile butadiene styrene mount. The distance between the metal plate and the pulsed coil can be adjusted by replacing the spacers.

The pump beam is emitted from an extended cavity diode laser (Toptica DL pro) and tuned to the D_1 line using an auxiliary Cs reference cell. A portion of the pump beam is used for saturated absorption spectroscopy to lock the laser frequency onto the $F = 3 \rightarrow F' = 4$ transition of the Cs cell, as shown in Fig. 2(b). Another portion of the pump beam is directed into an acousto-optic modulator (AOM_2, ISOMET M1205-9806-1) for intensity modulation. The same arbitrary-function generator controls both AOM_2 and the pulsed coil, with its two channels synchronized to switch the pump beam and pulsed magnetic field on and off simultaneously. The modulated laser beam is expanded to a waist diameter of 8 mm ($1/e^2$) through a beam expander. The combination of a half-wave plate (HP_6) and a polarization beam splitter (PBS_5) allows adjustment of the intensity of the pump beam. The linearly polarized pump beam then passes through a quarter-wave plate (QP) to convert it into circularly polarized light. Before entering the Cs vapor cell, the pump beam reaches a peak power of 0.75 mW, passes through the center of the pulsed coil, and is ultimately blocked by the metal plate.

In the path of the probe light, another extended cavity diode laser emits a probe beam tuned to the Cs D_2 transition line. The amplitude of the FID signal is optimized by adjusting the laser frequency, with the probe beam blue detuned by 400 MHz from the $F = 4 \rightarrow F' = 5$ transition, as shown in Fig. 2(b). A dichroic-atomic-vapor laser lock stabilizes the frequency of the probe beam. The frequency-stabilized beam passes through AOM_1, and its polarization fluctuations are

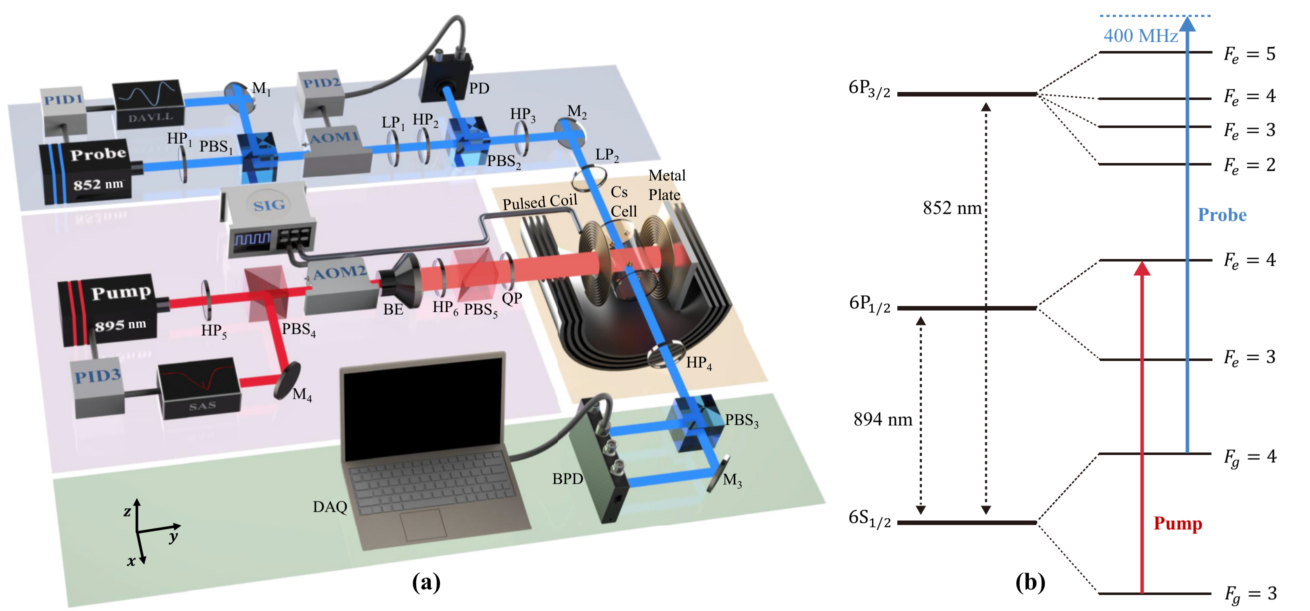

FIG. 2. (a) Schematic diagram of the enhanced-optical-pumping FID magnetometer for PECT. Definitions: AOM_1 and AOM_2, acousto-optic modulators; M_1, M_2, M_3, and M_4, mirrors; BE, beam expander; HP_1, HP_2, HP_3, HP_4, HP_5, and HP_6, half-wave plates; PBS_1, PBS_2, PBS_3, PBS_4, and PBS_5, polarization beam splitters; QP, quarter-wave plate; PD, InGaAs amplified photodetector; BPD, amplified balanced photodetector; PID_1, PID_2, and PID_3, proportional-integral-derivative controllers; LP_1 and LP_2, linear polarizers; DAVLL, dichroic-atomic-vapor laser lock; SAS, saturated absorption spectroscopy; DAQ, data acquisition. (b) Energy-level diagram of hyperfine transitions for the pump and probe beams. The pump beam is tuned to the transition of $F = 3 \rightarrow F' = 4$ (red line). The probe beam is blue detuned by 400 MHz from the $F = 4 \rightarrow F' = 5$ transition (blue line).

converted into power fluctuations via a linear polarizer (LP_1). A half-wave plate (HP_2) and a polarization beam splitter (PBS_2) split the probe beam into two portions. One beam is used for magnetic field measurements, while the other is focused onto an amplified photodetector (Thorlabs PDA20C) for laser-power stabilization through the combined use of a proportional-integral-derivative controller (PID_2, Stanford Research Systems SIM960) and AOM_1. The half-wave plate (HP_3) and linear polarizer (LP_2) are used to adjust the intensity and polarization axis of the power-stabilized probe beam, which is set to a power of 0.15 mW before entering the vapor cell. After passing through the Cs vapor cell, the probe beam's polarization axis is periodically modulated. An optical polarization-rotation detection system, comprising a half-wave plate (HP_4), a polarizing beam splitter (PBS_3), and an amplified balanced photodetector (Thorlabs PDB210A), is employed to extract variations in the polarization-rotation angle. The data-acquisition device (NI USB-6361) samples signals from the balanced polarimeter at $f_s = 800\,\text{kHz}$ with 16-bit voltage resolution. The differential signal associated with polarization rotation can be expressed as [41]

$$V_{\text{diff}} = V_1 - V_2 = V_0 \sin(2\theta), \tag{3}$$

where V_0 is the maximum voltage produced by the full intensity of the probe beam and θ is the polarization-rotation angle. The rotation angle θ is proportional to the transverse spin polarization $S_x(t)$ from Eq. (2) and can be written as

$$\theta = \theta_0 \sin(\omega_L t) \exp(-\Gamma t), \tag{4}$$

where θ_0 depends on factors such as atomic number density and optical path length [42]. Substituting Eq. (4) into Eq. (3) and applying the small-angle approximation yields the FID signal

$$V_{\text{diff}} \approx A \sin(\omega_L t) \exp(-\Gamma t), \tag{5}$$

where A is the amplitude of the FID signal.

Since the eddy-current magnetic field information is encoded in the oscillation frequency of the FID signal, the phase $\phi(t)$ can be extracted from the FID signal using the instantaneous phase-retrieval method [35]. The total magnetic field consists of the eddy-current magnetic field and the bias magnetic field, so its vector magnitude can be written as $B_{\text{tot}} = \sqrt{B_{\text{ec}}^2 + 2B_{\text{ec}}B_0\cos(\alpha) + B_0^2}$, where α is the angle between the eddy-current field and the bias field. Accordingly, the phase of the FID signal is

$$\phi(t) = \gamma B_{\text{tot}} t = \gamma \sqrt{B_{\text{ec}}^2 + 2B_{\text{ec}}B_0\cos(\alpha) + B_0^2}\, t. \tag{6}$$

Because the magnitude of the eddy-current magnetic field is much smaller than that of the bias field B_0, we apply a Taylor expansion to Eq. (6) to obtain

$$\phi(t) \approx \gamma B_0 t + \gamma B_{\text{ec}} \cos(\alpha) t + \gamma \frac{B_{\text{ec}}^2 \sin^2(\alpha)}{2B_0} t. \tag{7}$$

We select $\alpha = \pi/2$ as a typical value in our experimental setup, so Eq. (7) simplifies to $\phi(t) \approx \gamma B_0 t + \gamma (B_{\text{ec}}^2/2B_0)t$. Since the eddy-current magnetic field decays approximately exponentially over time [43], the total phase can be analyzed using both linear and nonlinear fitting. A linear fit directly yields the bias field B_0, whereas a nonlinear fit reveals the decay profile of B_{ec}. The exponential time constant τ obtained from the nonlinear fit defines the eddy-current decay time, enabling determination of intrinsic metal properties such as electrical conductivity, permeability, and thickness.

III. RESULTS AND DISCUSSION

A. Signal analysis and performance analysis

Figure 3 shows the raw experimental signal obtained using the enhanced-optical-pumping scheme, with a pump duration of 4 ms and a probe duration of 16 ms. The results show that this enhanced-optical-pumping strategy enables the magnetometer to acquire FID signals with high signal-to-noise ratio (SNR) compared to signals measured without pulsed magnetic-field enhancement. To illustrate the capability of this magnetometer in reconstructing an ac magnetic field, a sinusoidal modulation field $B_m(t) = \Delta B \cos(2\pi f_m t + \phi_m)$ is applied along the bias field direction. The polarization-rotation signal can be expressed as [35]

$$S_x(t) = A(t) \cos(\omega_0 t + \beta \sin(2\pi f_m t + \phi_m) + \phi_0), \tag{8}$$

where $A(t)$ is the envelope of the FID signal, ω_0 is the Larmor frequency, f_m is the modulation frequency, and $\beta = \gamma \Delta B / 2\pi f_m$ is the modulation index, representing the amplitude of the instantaneous residual phase oscillation. Both ϕ_m and ϕ_0 are initial phases.

The instantaneous phase of the FID signal is extracted using the Hilbert transform [44]. As shown in Fig. 4(a), the cumulative phase is linearly fitted to determine the magnitude of the dc magnetic field from the slope. By subtracting this linear fit from the cumulative phase, we obtain the residual phase, which corresponds to the phase accumulated by the modulated magnetic field. From the residual phase, the modulation frequency f_m and modulation index β are extracted, allowing calculation of the modulated magnetic field amplitude ΔB. The frequency response of the magnetometer is characterized by comparing the oscillating field amplitude ΔB obtained via instantaneous phase retrieval with the value B_{coil} generated by a coil. The ratio of the measured values over a 10 kHz modulation-frequency range is shown in Fig. 4(b), where the dc field is 5 μT and the modulation field amplitude is 50 nT. The −3 dB bandwidth of the magnetometer is estimated to be 4.2 kHz, ultimately limited by the measurement SNR.

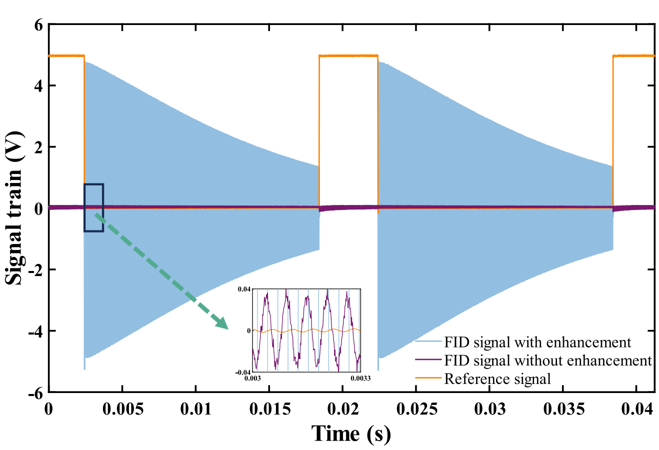

FIG. 3. Polarimeter-detected FID traces measured in an ambient field of 5 μT. FID signal trains with the enhanced-optical-pumping strategy (blue line) and without enhancement (purple line) are shown to illustrate the effect of the enhancement. The pump-probe repetition time is set to 20 ms (orange line).

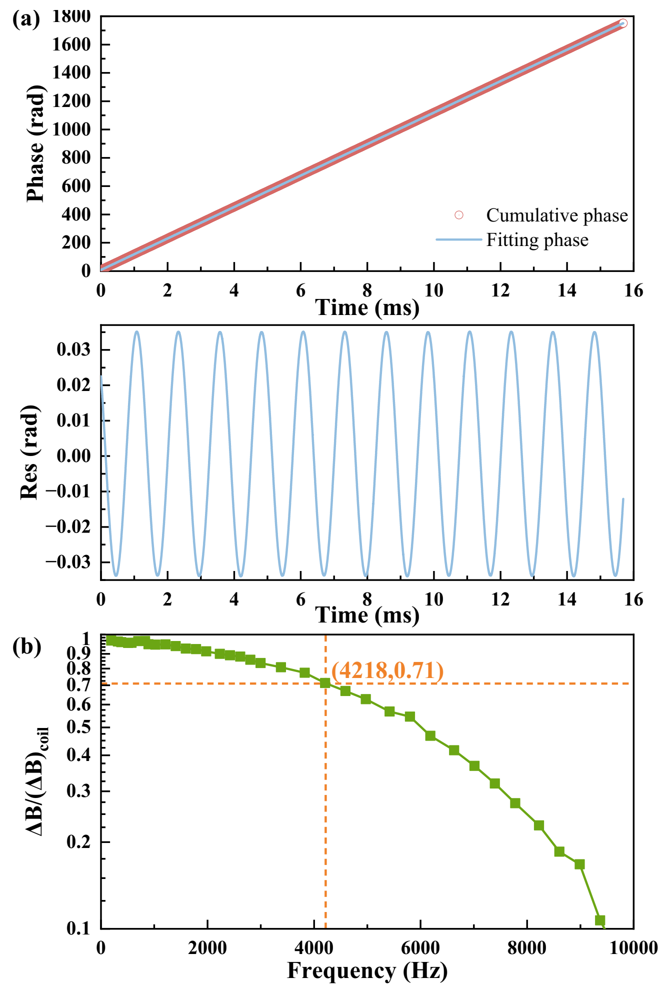

FIG. 4. (a) Instantaneous phase $\varphi_I(t)$ retrieved from the FID signal under an additional modulated magnetic field. Linear regression of $\varphi_I(t)$ gives a slope of $d\varphi_I/dt = 111.104$ rad/ms, corresponding to a Larmor frequency of 17.683 kHz and a dc magnetic-field strength of $B_0 = 5.052$ μT. The residual from the linear fit shows a sinusoidal modulation, from which we extract a modulation frequency $f_m = 800$ Hz and a modulation index $\beta = 0.035$ rad, corresponding to an ac magnetic-field strength $\Delta B = 50.26$ nT. (b) Frequency response of the FID magnetometer using the instantaneous phase-retrieval method, with the −3 dB bandwidth estimated as 4.2 kHz, indicated by the dashed lines.

The magnetic sensitivity of instantaneous phase retrieval is ultimately determined by the ability to resolve small changes in the instantaneous phase. A representative amplitude spectral density of the instantaneous phase $\sqrt{S_{\phi(f)}}$ is shown in Fig. 5, indicating a white-noise floor with a magnitude of 0.53 $\mu\text{rad}/\sqrt{\text{Hz}}$. The magnetic field noise $\sqrt{S_B(f)}$ can be derived from the instantaneous phase noise via $\sqrt{S_B(f)} = f/\gamma \sqrt{S_\phi(f)}$, yielding a magnetic field noise spectral density (NSD) of 0.45 $\text{pT}/\sqrt{\text{Hz}}$. Notably, limited by the frequency resolution, spectral leakage tends to make the noise peak less distinct. Since the time-domain magnetic field is calculated

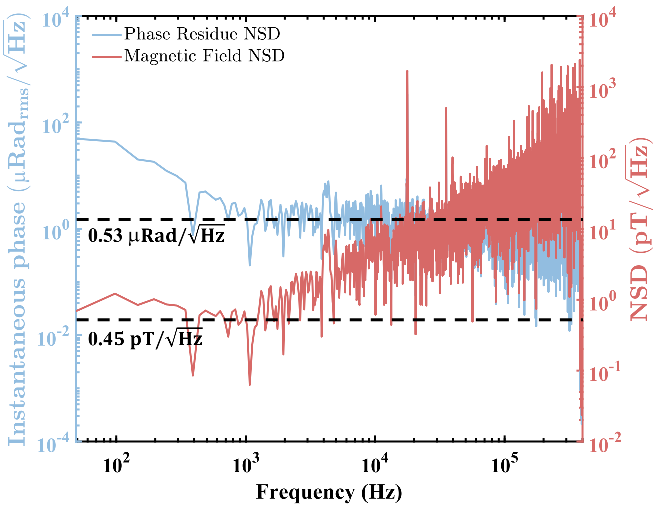

FIG. 5. The amplitude of the measured magnetic field is 5 μT. The amplitude spectral density of the instantaneous phase $\sqrt{S_\phi(f)}$ (blue line) and the corresponding magnetic field noise spectral density $\sqrt{S_B(f)}$ (red line) of the FID magnetometer are also shown.

from the derivative of the phase, after Fourier transformation, the NSD of the magnetic field in the frequency domain is equal to the amplitude spectral density of the phase multiplied by the frequency [35]. Consequently, the noise floor of the magnetic field increases with frequency, causing the sensitivity of the magnetometer to deteriorate at higher frequencies.

B. Transient-magnetic-field measurement and time-constant extraction

We analyze the FID signals acquired with and without the metal plate in the magnetometer system, as shown in Fig. 6. Interestingly, we observe that when a metal plate is present, the FID signal exhibits a significantly higher relaxation rate in its initial phase. This phenomenon arises from the transverse relaxation of spin polarization, which is induced by the magnetic field gradient generated by the eddy-current magnetic field [45]. As the eddy-current magnetic field decays, the associated gradient diminishes, leading to a progressive weakening of the gradient-induced transverse spin relaxation. Once the eddy-current magnetic field has fully decayed, the transverse relaxation rate of the FID signal in the presence of the metal plate reverts to a rate consistent with that observed without the plate. Furthermore, the introduction of the eddy-current magnetic field changes the total field direction, modifying the projection of the magnetic moment along the probe beam. This results in a decreased amplitude of the FID signal compared to the configuration without the metal plate.

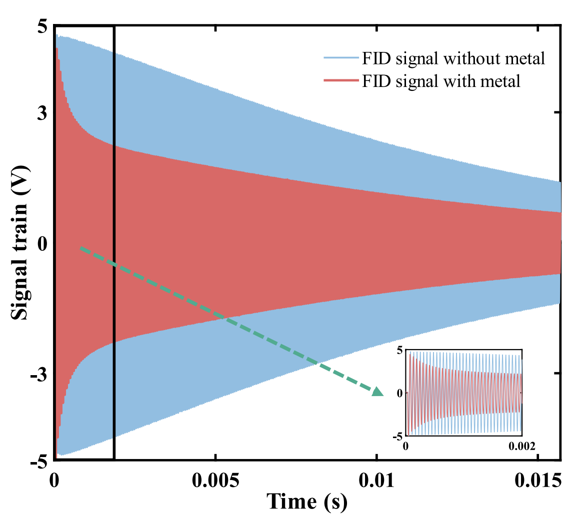

FIG. 6. Sample FID signal train acquired by the polarimeter in an ambient field of 5 μT. The signals obtained without metal (blue line) and with metal (red line) are shown to illustrate the effect of the eddy-current magnetic field.

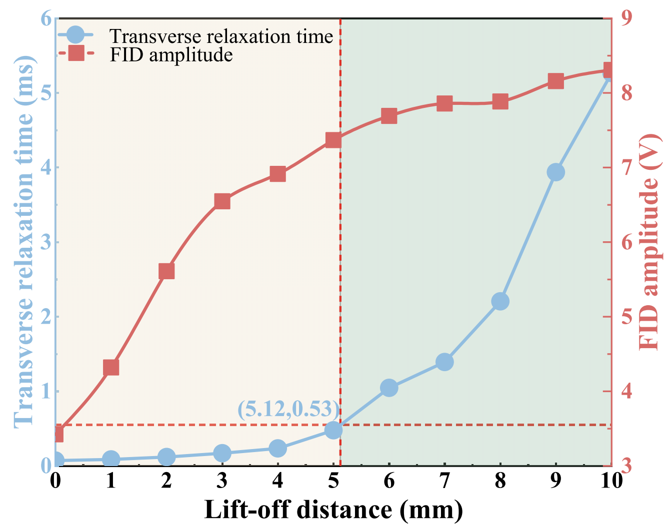

FIG. 7. Effect of the eddy-current magnetic field on the FID signal. Variation of the transverse relaxation time (blue line) and FID signal amplitude (red line) with lift-off distance. The green shaded area indicates the FID signal transverse relaxation time exceeding the eddy-current characteristic time, while the pale beige area represents the opposite. The test material is a zinc plate with the thickness of 5 mm. The values of μ_0 and σ are $4\pi \times 10^{-7}$ H/m and 1.7×10^7 S/m, respectively.

To further examine the influence of the eddy-current magnetic field on the FID signal, we adjusted the distance between the metal plate and the pulsed coil to vary the strength of the eddy-current magnetic field. The amplitude and transverse relaxation time are extracted from the initial FID signals using the Levenberg-Marquardt algorithm [46], demonstrating their dependence on the lift-off distance. As shown in Fig. 7, increasing lift-off distance will attenuate the induced eddy-current magnetic field. This attenuation reduces gradient-induced transverse spin relaxation effects, extending the transverse relaxation time of the FID signal. Simultaneously, the weaker eddy-current magnetic field mitigates its directional influence on the total magnetic field. This is reflected in the amplitude term $\sqrt{B_0^2/(B_0^2+B_{\rm ec}^2)}$ in Eq. (2): as the eddy-current magnetic field decreases, the vector resultant field diminishes, thereby increasing the amplitude of the FID signal. Furthermore, the characteristic time τ of the eddy-current magnetic field can be estimated using the

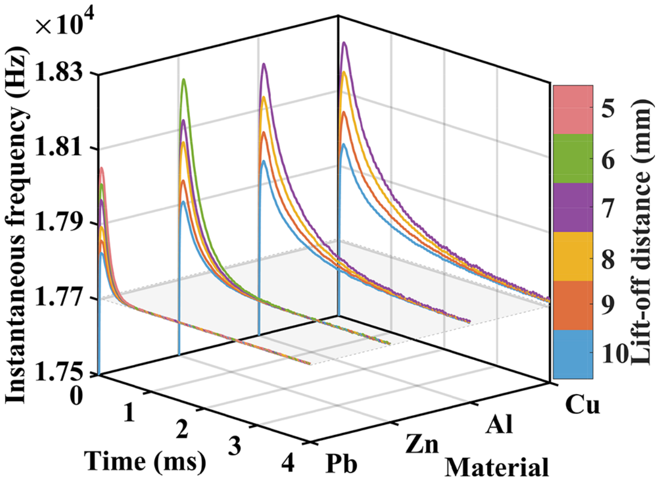

FIG. 8. The response of the instantaneous frequency of the FID signal is investigated for four 10-mm-thick metals across a range of lift-off distances. Planes along the y axis represent different metal types, arranged from outermost to innermost as Pb, Zn, Al, and Cu. Different colored lines represent different lift-off distances: 5 mm (red line); 6 mm (green line); 7 mm (purple line); 8 mm (yellow line); 9 mm (orange line); and 10 mm (blue line). The gray plane denotes the Larmor frequency of the ambient magnetic field to which the instantaneous frequency of the FID signal asymptotically converges.

expression [47]

$$\tau \sim L^2 \mu_0 \sigma, \tag{9}$$

where L is the thickness of the metal plate, μ_0 is the permeability of the metal, and σ denotes the electrical conductivity. For example, for a 5-mm-thick zinc plate, with $\mu_0 = 4\pi \times 10^{-7}$ H/m and $\sigma = 1.7 \times 10^7$ S/m, the characteristic time of the eddy-current magnetic field is predicted to be 0.53 ms. The FID signal can adequately capture the temporal evolution of the eddy-current magnetic field only if its transverse relaxation time is longer than the characteristic time. For this reason, we define the corresponding lift-off distance as the effective working distance, which is indicated by the green shaded area in the Fig. 7. To extract the instantaneous phase information, the Hilbert transform is applied to the FID signal (red line) shown in Fig. 6. The instantaneous phase is a superposition of contributions from both the static bias magnetic field B_0 and the eddy-current magnetic field B_{ec}. The instantaneous frequency is then obtained by differentiating the instantaneous phase with respect to time [48], providing the temporal variation of the total external magnetic field captured by the FID signal. Considering the effective working distances discussed above, the instantaneous frequencies of the FID signals for different metallic materials at various lift-off distances are plotted in Fig. 8. The instantaneous frequency extracted from all four metal types exhibits a similar temporal evolution: a rapid initial increase, followed by exponential decay, and eventually stabilizing at a steady-state value. In all cases, the instantaneous frequency converges to the Larmor frequency of the static bias magnetic field B_0. This observed magnetic field behavior is consistent with the eddy-current magnetic field variations detected by Hall sensors in PECT [10,49]. To further verify the variation pattern of the pulsed-eddy-current magnetic field, we apply the Extended Truncated Region Eigenfunction Expansion (ETREE) method [49] to perform numerical simulations of the pulsed-eddy-current magnetic field (seeing Appendix A for details). As shown in Fig. 10, good overall agreement is observed between the normalized experimental and simulation results. The minor observed discrepancies can be attributed to the approximations employed in Eq. (7).

The initial lift-off distance varies according to differences in electrical conductivity among the metals, as illustrated in Fig. 7. From the comparisons in Fig. 8, it is evident that for a given metal, a smaller lift-off distance—indicating closer proximity between the metal plate and the pulsed coil—produces a stronger eddy-current magnetic field. This is reflected in a higher peak value of the instantaneous frequency. At a fixed lift-off distance, metals with higher electrical conductivity generate stronger eddy-current magnetic fields, resulting in a higher peak frequency. Additionally, increased conductivity extends the decay time constant of the eddy-current field. These observations are consistent with established principles governing eddy-current magnetic fields [50].

After subtracting the linearly fitted phase contribution of the static bias field B_0, we obtain the residual phase, which corresponds to the contribution of the eddy-current magnetic field to phase accumulation. To account for the minor bias-field phase residual originating from approximations in Eq. (7), we use a combined fitting model comprising both linear and exponential components. This approach yields a goodness of fit of $R^2 = 0.998$ and allows extraction of the characteristic time constant τ of the eddy-current field from the exponential term [43]. The fitting results for metals of different materials and thicknesses are presented in Fig. 9, revealing several key observations. For a given metal and

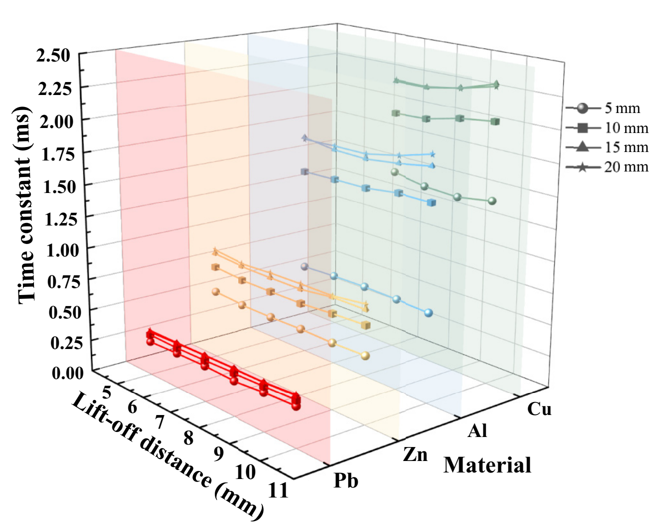

FIG. 9. Estimation of the eddy-current magnetic field time constants for various metals, thicknesses, and lift-off distances. The red (Pb), beige (Zn), blue (Al), and green (Cu) planes represent different metals. The plate thickness is indicated by geometric symbols: spheres (5 mm), cubes (10 mm), tetrahedrons (15 mm), and pentahedrons (20 mm).

thickness, the characteristic time constant of the eddy-current field remains constant as the lift-off distance varies. Since the decay behavior of the eddy-current field depends only on intrinsic properties of the metal, such as electrical conductivity, permeability, and thickness, it is therefore independent of lift-off distance. Meanwhile, for metals of the same thickness but different electrical conductivities, the time constant shows a positive correlation with electrical conductivity, indicating a slower decay of the eddy-current magnetic field in more conductive metals. Moreover, for a given metal, the time constant increases with thickness until it approaches the skin depth. Once the thickness exceeds the skin depth, the time constant remains nearly unchanged, as the diffusion of the eddy-current fields is primarily confined to the skin-depth region. These experimental observations are consistent with the behavior of eddy-current magnetic fields in nondestructive testing [51].

IV. CONCLUSIONS AND OUTLOOK

In conclusion, we have proposed an alternative approach for PECT in transient electromagnetic measurements, using a free-induction-decay magnetometer to detect and characterize eddy-current magnetic fields. The central feature of this approach is the use of a pulsed magnetic field during the pumping stage, which plays a dual role: It not only significantly improves the polarization of the atomic ensemble to amplify the FID signal and improve sensitivity, but also acts as an excitation source to induce eddy-current magnetic fields. The FID magnetometer achieves a noise floor of 0.45 $\mathrm{pT}/\sqrt{\mathrm{Hz}}$ and a bandwidth of 4.2 kHz. Its combination of high bandwidth and strong robustness allows for multifrequency component detection in the induced magnetic field. Moreover, the FID magnetometer in our scheme removes the need for complex closed-loop feedback circuits, making miniaturization and system integration more straightforward for practical applications.

It should be noted that the theoretical model adopted in this work is a simplified version, and solving the full Bloch equations for complex, time-varying magnetic field configurations remains a challenge for future research. Nevertheless, the simplified model used here demonstrates that eddy-current magnetic field information can be effectively extracted from the instantaneous phase of the FID signal, producing excellent fitting results. Furthermore, the pulsed-eddy-current magnetic fields obtained from normalized numerical fitting based on the ETREE method exhibit good overall agreement with the experimentally measured normalized fields. For applications in unshielded environments, such as mineral exploration with transient electromagnetic method, strategies like compensation for geomagnetic diurnal variations could be adopted to calibrate the PECT system. The proposed PECT approach holds considerable potential for applications including magnetic induction tomography [52] and remote-field eddy-current testing [53,54].

ACKNOWLEDGMENTS

We acknowledge Shuyuan Chen, Xingqing Jin, and Wenlong Lyu for assisting with the antirelaxation-coated vapor cells for this work. This work was supported by the Deep-Earth Probe and Mineral Resources Exploration—National Science and Technology Major Project of China (Grant No. 2025ZD1011400).

DATA AVAILABILITY

The data that support the findings of this article are not publicly available upon publication because it is not technically feasible and/or the cost of preparing, depositing, and hosting the data would be prohibitive within the terms of this research project. The data are available from the authors upon reasonable request.

APPENDIX A: NUMERICAL SIMULATION OF THE PULSED-EDDY-CURRENT MAGNETIC FIELD

This Appendix presents the numerical simulation process of the pulsed-eddy-current magnetic field shown in Fig. 10. Since a transient signal can be theoretically represented by superimposing a series of sinusoidal harmonics in the frequency domain, the PEC signal for a metal plate is derived from a superposition of harmonic responses from the sample in the frequency domain via the inverse Fourier transform. By applying the ETREE method with an appropriately defined truncation region and replacing complex integral expressions with series expansions [49], the formula can be simplified to

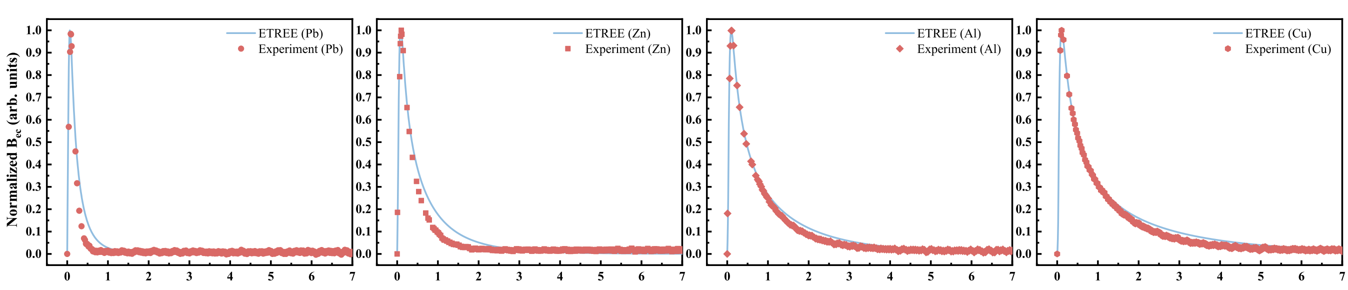

FIG. 10. The normalized pulsed-eddy-current magnetic fields (blue lines) obtained from numerical simulations using the ETREE method are compared with normalized experimental data (red points). The experimental points for Pb, Zn, Al, and Cu are represented by circles, squares, diamonds, and hexagons, respectively.

TABLE I. The experimental parameters employed in numerical simulation of the pulsed-eddy-current magnetic field.

Parameter	Value	Parameter	Value	Parameter	Value	Parameter	Value
N[a]	20	L_{sensor}	35 mm	r_1	5 mm	σ_{air}	0 S/m
I_{coil}	49.6 mA	W_{sensor}	25 mm	r_2	13.75 mm	σ_{Pb}	4.8×10^6 S/m
L_{coil}	0.1 mm	T_{sensor}	25 mm	f_0[b]	50 Hz	σ_{Zn}	1.7×10^7 S/m
Duty cycle	20%	Z_{sensor}	22.25 mm	μ_r^{air}	1	σ_{Al}	3.4×10^7 S/m
Lift-off Distance	10 mm	T_{metal}[c]	10 mm	μ_r^{Al}	1	σ_{Cu}	5.8×10^7 S/m

[a]The number of turns of the coil.
[b]The driving frequency of the current.
[c]The thickness of the metal plate.

the following expression:

$$
\begin{aligned}
B(t) &= B_{\mathrm{p}}(t) + B_{\mathrm{ec}}(t) = \frac{1}{\pi}\int_{-\infty}^{+\infty}\left[B_{\mathrm{p}}(\omega) + B_{\mathrm{ec}}(\omega)\right]e^{j\omega t}\,d\omega,\\
B_{\mathrm{p}}(t) &= \frac{2\mu_0 i_0(t)}{r_0(c_2-c_1)}\sum_{i=1}^{\infty}\frac{J_1(a_i r_0)\chi(a_i r_1, a_i r_2)}{a_i^4[hJ_0(a_i h)]^2}\times\int_{c_1}^{c_2}F(a_i z_1, a_i z_2, a_i z)\mathrm{d}z,\\
B_{\mathrm{ec}}(t) &= \frac{2\mu_0}{\pi r_0(c_2-c_1)}\sum_{i=1}^{\infty}\frac{J_1(a_i r_0)\chi(a_i r_1, a_i r_2)}{a_i^5[hJ_0(a_i h)]^2}(e^{-a_i c_2}-e^{-a_i c_1})(e^{-a_i z_2}-e^{-a_i z_1})\int_{-\infty}^{+\infty} i_0(\omega)\frac{V_1}{U_1}e^{j\omega t}\,d\omega,
\end{aligned}
\tag{A1}
$$

where $B_{\mathrm{p}}(t)$ is the magnetic field generated by the pulsed coil and $B_{\mathrm{ec}}(t)$ is the eddy-current magnetic field induced by the metallic conductor. a_i represents the characteristic roots satisfying $J_0(ha_i) = 0$ and h is the truncation distance. The current source density $i_0(t)$ is expressed as $i_0(t) = NI(t)/[(r_2 - r_1)(z_2 - z_1)]$, where r_1 and r_2 are the inner and outer radii of the coil, and z_1 and z_2 are the distances from the lower and upper surfaces of the coil to the metal plate, respectively. c_1 and c_2 represent the distances from the lower and upper surfaces of the sensor to the metal plate, and $J_0(x)$ and $J_1(x)$ are the zero-order and first-order Bessel functions, respectively. The remaining terms comprise the Fourier transform of the current function, the position function, and the integral function, which can be expressed as

$$
i_0(t) = \frac{1}{\pi}\int_{-\infty}^{+\infty} i_0(\omega)e^{j\omega t}\,d\omega,
\tag{A2}
$$

$$
\chi(x_1, x_2) = \int_{x_1}^{x_2} xJ_1(x)\mathrm{d}x,
\tag{A3}
$$

$$
F(a_i z_1, a_i z_2, a_i z) = \begin{cases} \mathrm{e}^{a_i(z_2-z)} - \mathrm{e}^{a_i(z_1-z)}, & z \geqslant z_2,\\ 2 - \mathrm{e}^{a_i(z-z_2)} - \mathrm{e}^{a_i(z_1-z)}, & z_2 \geqslant z \geqslant z_1,\\ \mathrm{e}^{a_i(z-z_1)} - \mathrm{e}^{a_i(z-z_2)}, & z_1 \geqslant z. \end{cases}
\tag{A4}
$$

$\mathrm{V}_1/\mathrm{U}_1$ represents the reflection coefficient, which acts as a spatial frequency filter governing the magnitude of the eddy-current magnetic field generated at different excitation frequencies. For the conductor with L layers, σ_L and μ_L represent the electrical conductivity and magnetic permeability of the corresponding metal layer, respectively. The thickness of each layer is given by $d_j - d_{j-1}$, where the subscript j ranges from $L - 1$ to 1. The reflection coefficient can be expressed via a recursive formula as

$$
\begin{aligned}
U_j &= \left(\frac{\alpha_{j-1}}{\mu_{j-1}} - \frac{\alpha_j}{\mu_j}\right)\mathrm{e}^{-2\alpha_j(d_j-d_{j-1})}V_{j+1} + \left(\frac{\alpha_{j-1}}{\mu_{j-1}} + \frac{\alpha_j}{\mu_j}\right)U_{j+1},\\
V_j &= \left(\frac{\alpha_{j-1}}{\mu_{j-1}} + \frac{\alpha_j}{\mu_j}\right)\mathrm{e}^{-2\alpha_j(d_j-d_{j-1})}V_{j+1} + \left(\frac{\alpha_{j-1}}{\mu_{j-1}} - \frac{\alpha_j}{\mu_j}\right)U_{j+1},\\
U_L &= \frac{\alpha_{L-1}}{\mu_{L-1}} + \frac{\alpha_L}{\mu_L}, \qquad V_L = \frac{\alpha_{L-1}}{\mu_{L-1}} - \frac{\alpha_L}{\mu_L},\\
\alpha_L &= \sqrt{a_i^2 + \mathrm{j}\omega\mu_0\mu_L\sigma_L}, \quad \alpha_0 = a_i.
\end{aligned}
\tag{A5}
$$

By using the parameters listed in Table I and performing numerical simulations, we theoretically derive the variation trend of the pulsed-eddy-current magnetic field. Meanwhile, differentiating the residual phase enables us to determine the time evolution of the eddy-current magnetic field with the bias magnetic field B_0 eliminated. Due to the scaling factor associated with the eddy-current magnetic field in Eq. (7), both the theoretical curves and experimental data are

TABLE II. Skin depth at the first and third harmonic frequencies for different metals.

Material	Frequency (Hz)	Skin depth (mm)
Pb	50/150	32.49/18.76
Zn	50/150	17.26/9.97
Al	50/150	12.21/7.05
Cu	50/150	9.35/5.40

normalized to enable clearer comparison of their profile variations. As shown in Fig. 10, we compare the theoretical and experimentally measured pulsed-eddy-current magnetic fields for the four metal plates (Pb, Zn, Al, Cu), each with a thickness of 10 mm and a lift-off distance of 10 mm. The results indicate that for four metals, the theoretically simulated eddy-current magnetic fields are in good overall agreement with the experimentally measured data. The minor observed discrepancies can be attributed to the approximations employed in Eq. (7).

APPENDIX B: QUANTITATIVE THICKNESS ANALYSIS OF METALLIC PLATES BASED ON PULSED-EDDY-CURRENT MAGNETIC FIELD SIGNALS

We attempt to perform a quantitative analysis of metallic plate thickness based on the pulsed-eddy-current magnetic field signals detected by the FID magnetometer. Since the lift-off distance is usually coupled into the pulsed-eddy-current magnetic field signal, its influence must be minimized before quantitative inversion can be carried out. In principle, after transforming the pulsed-eddy-current magnetic fields into the frequency domain, the phase at the odd harmonics of the excitation frequency is insensitive to the lift-off distance [55]. According to the skin-depth formula

$$\delta = \frac{1}{\sqrt{\pi f \mu \sigma}}, \tag{B1}$$

where f is the excitation frequency, μ is the magnetic permeability, and σ is the electrical conductivity, we calculate the skin depth of different metals at the first and third excitation harmonic frequencies, as listed in Table II.

According to the analysis in Ref. [55], thickness estimation is expected to be more accurate when the sample thickness is smaller than one-third of the skin depth. Based on this consideration, we selected the phase of the lead sample at the first excitation harmonic frequency for a preliminary thickness estimation. Using the theoretical framework given in Appendix A, we theoretically obtained the corresponding phase-thickness relationship for the lead plate at the first excitation harmonic frequency, as shown in Fig. 11.

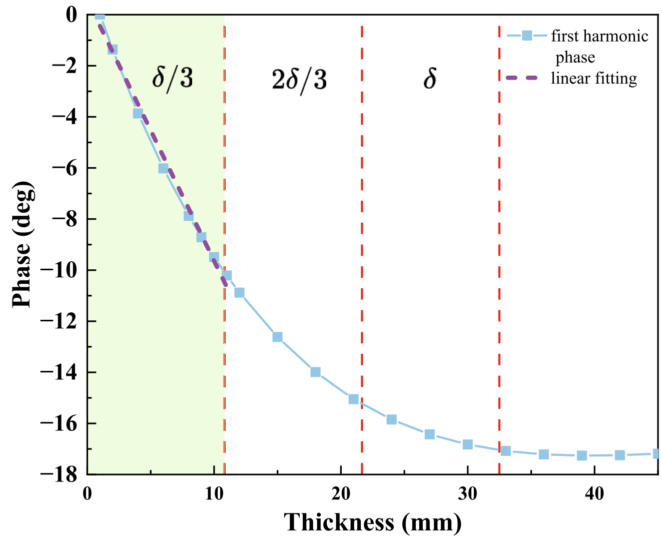

FIG. 11. Variation of the first harmonic phase with metal thickness. The theoretically calculated phase thickness relationship for the first harmonic (blue line), and the linear fitting curve used for thickness estimation (purple line).

The green shaded region denotes the range where the thickness is smaller than one-third of the skin depth. This region serves as the approximately linear interval for thickness estimation, as indicated by the purple line segment in Fig. 11. We select the phase values at the first excitation harmonic from the experimentally measured instantaneous pulsed-eddy-current magnetic field responses of the 5 and 10 mm lead plates, which are 12.27° and 8.56°, respectively. Considering the influence of power-line noise in the measured signal, these values require recalibration. According to the linear fitting result, the corrected phase for the 5 mm lead plate is 4.35°, indicating that the phase contribution introduced by power-line noise is approximately 16.8°. After removing the contribution of power-line noise, the corrected phase for the 10 mm lead plate is estimated to be 8.24°. Using the linear fitting relation, the corresponding plate thickness is estimated to be 8.64 mm, with an error of 13.6%.

These results indicate that quantitative inversion for metallic plates is feasible to a certain extent. The estimation error is likely associated with the measurement uncertainty of the pulsed eddy-current magnetic field, as well as the unavoidable influence of power-line noise in the present experiment. In future work, the inversion accuracy may be further improve by reducing experimental errors, optimizing signal processing, and exploring alternative thickness-estimation methods, such as the lift-off intersection method [56] and feature extraction methods [57].

[1] J. García-Martín, J. Gómez-Gil, and E. Vázquez-Sánchez, Non-destructive techniques based on eddy current testing, Sensors **11**, 2525 (2011).

[2] Y. He, F. Luo, M. Pan, F. Weng, X. Hu, J. Gao, and B. Liu, Pulsed eddy current technique for defect detection in aircraft riveted structures, NDT&E Int. **43**, 176 (2010).

[3] A. Sophian, G. Tian, and M. Fan, Pulsed eddy current non-destructive testing and evaluation: A review, Chin. J. Mech. Eng. **30**, 1474 (2017).

[4] G. Xue, X. Wu, W. Chen, and N. Zhou, Grounded-source short offset transient electromagnetic method: Theory and applications in deep mineral exploration, Sci. China: Earth Sci. **68**, 626 (2025).
[5] Z. Guo, G. Xue, J. Liu, and X. Wu, Electromagnetic methods for mineral exploration in China: A review, Ore Geol. Rev. **118**, 103357 (2020).
[6] Y. Das, J. E. McFee, J. Toews, and G. C. Stuart, Analysis of an electromagnetic induction detector for real-time location of buried objects, IEEE Trans. Geosci. Remote Sens. **28**, 278 (1990).
[7] L. Wang, S. Zhang, S. Chen, and H. Jiang, Fast characterization for UXO-like targets with a portable transient electromagnetic system, Measurement **189**, 110492 (2022).
[8] S. Chen, S. Zhang, J. Zhu, and X. Luan, Accurate measurement of characteristic response for unexploded ordnance with transient electromagnetic system, IEEE Trans. Instrum. Meas. **69**, 1728 (2019).
[9] R. A. Smith and G. R. Hugo, Transient eddy-current NDE for ageing aircraft: Capabilities and limitations, Insight **43**, 14 (2001).
[10] J. Bowler and M. Johnson, Pulsed eddy-current response to a conducting half-space, IEEE Trans. Magn. **33**, 2258 (1997).
[11] G. Y. Tian and A. Sophian, Study of magnetic sensors for pulsed eddy current techniques, Insight **47**, 277 (2005).
[12] G. Panaitov, H.-J. Krause, and Y. Zhang, Pulsed eddy current transient technique with HTS SQUID magnetometer for non-destructive evaluation, Physica C **372–376**, 278 (2002).
[13] I. K. Kominis, T. W. Kornack, J. C. Allred, and M. V. Romalis, A subfemtotesla multichannel atomic magnetometer, Nature (London) **422**, 596 (2003).
[14] H. B. Dang, A. C. Maloof, and M. V. Romalis, Ultrahigh sensitivity magnetic field and magnetization measurements with an atomic magnetometer, Appl. Phys. Lett. **97**, 151110 (2010).
[15] D. Budker and M. Romalis, Optical magnetometry, Nat. Phys. **3**, 227 (2007).
[16] D. Budker and D. F. J. Kimball, *Optical Magnetometry* (Cambridge University Press, Cambridge, 2013).
[17] A. M. Akulshin, D. Budker, F. P. Bustos, T. Dang, E. Klinger, S. M. Rochester, A. Wickenbrock, and R. Zhang, Remote detection optical magnetometry, Phys. Rep. **1106**, 1 (2025).
[18] T. M. Tierney, N. Holmes, S. Mellor, J. D. López, G. Roberts, R. M. Hill, E. Boto, J. Leggett, V. Shah, M. J. Brookes, R. Bowtell, and G. R. Barnes, Optically pumped magnetometers: From quantum origins to multi-channel magnetoencephalography, NeuroImage **199**, 598 (2019).
[19] E. Boto, N. Holmes, J. Leggett, G. Roberts, V. Shah, S. S. Meyer, L. Duque Muñoz, K. J. Mullinger, T. M. Tierney, S. Bestmann, G. R. Barnes, R. Bowtell, and M. J. Brookes, Moving magnetoencephalography towards real-world applications with a wearable system, Nature (London) **555**, 657 (2018).
[20] M. E. Limes, E. L. Foley, T. W. Kornack, S. Caliga, S. McBride, A. Braun, W. Lee, V. G. Lucivero, and M. V. Romalis, Portable magnetometry for detection of biomagnetism in ambient environments, Phys. Rev. Appl. **14**, 011002(R) (2020).
[21] R. Zhang and R. Mhaskar, Advanced magnetometer system: Task II, Technical Report, Contract No. W912HQ-16-C-0010 and Project No. MR-2646, Geometrics, 2019.
[22] J. D. Zipfel, S. Santosh, P. Bevington, and W. Chalupczak, Object composition identification by measurement of local radio frequency magnetic fields with an atomic magnetometer, Appl. Sci. **12**, 8219 (2022).
[23] I. M. Savukov, S. J. Seltzer, and M. V. Romalis, Detection of NMR signals with a radio-frequency atomic magnetometer, J. Magn. Reson. **185**, 214 (2007).
[24] A. Wickenbrock, S. Jurgilas, A. Dow, L. Marmugi, and F. Renzoni, Magnetic induction tomography using an all-optical ^{87}Rb atomic magnetometer, Opt. Lett. **39**, 6367 (2014).
[25] Z. D. Grujić, P. A. Koss, G. Bison, and A. Weis, A sensitive and accurate atomic magnetometer based on free spin precession, Eur. Phys. J. D **69**, 135 (2015).
[26] D. Hunter, T. E. Dyer, and E. Riis, Accurate optically pumped magnetometer based on Ramsey-style interrogation, Opt. Lett. **47**, 1230 (2022).
[27] S. Ingleby, P. Griffin, T. Dyer, M. Mrozowski, and E. Riis, A digital alkali spin maser, Sci. Rep. **12**, 12888 (2022).
[28] D. Hunter, S. Piccolomo, J. D. Pritchard, N. L. Brockie, T. E. Dyer, and E. Riis, Free-induction-decay magnetometer based on a microfabricated Cs vapor cell, Phys. Rev. Appl. **10**, 014002 (2018).
[29] W. Gawlik and S. Pustelny, Nonlinear Faraday effect and its applications, in *New Trends in Quantum Coherence and Nonlinear Optics*, edited by R. Drampyan, Horizons in World Physics Vol. 263 (Nova Science Publishers, New York, 2009), p. 45.
[30] D. Hunter, R. Jiménez-Martínez, J. Herbsommer, S. Ramaswamy, W. Li, and E. Riis, Waveform reconstruction with a Cs-based free-induction-decay magnetometer, Opt. Express **26**, 30523 (2018).
[31] K. Yi, Y. Liu, B. Wang, W. Xiao, D. Sheng, X. Peng, and H. Guo, Free-induction-decay ^{4}He magnetometer using a multipass cell, Phys. Rev. Appl. **22**, 014084 (2024).
[32] D. Sheng, S. Li, N. Dural, and M. V. Romalis, Subfemtotesla scalar atomic magnetometry using multipass cells, Phys. Rev. Lett. **110**, 160802 (2013).
[33] W. E. Bell and A. L. Bloom, Optically driven spin precession, Phys. Rev. Lett. **6**, 280 (1961).
[34] J. C. Visschers, E. Wilson, T. Conneely, A. Mudrov, and L. Bougas, Rapid parameter determination of discrete damped sinusoidal oscillations, Opt. Express **29**, 6863 (2021).
[35] N. Wilson, C. Perrella, R. Anderson, A. Luiten, and P. Light, Wide-bandwidth atomic magnetometry via instantaneous-phase retrieval, Phys. Rev. Res. **2**, 013213 (2020).
[36] D. Hunter, M. S. Mrozowski, A. McWilliam, S. J. Ingleby, T. E. Dyer, P. F. Griffin, and E. Riis, Optical pumping enhancement of a free-induction-decay magnetometer, J. Opt. Soc. Am. B **40**, 2664 (2023).
[37] G. Bevilacqua, V. Biancalana, P. Chessa, and Y. Dancheva, Multichannel optical atomic magnetometer operating in unshielded environment, Appl. Phys. B **122**, 103 (2016).
[38] A. P. McWilliam, S. Dyer, D. Hunter, M. Mrozowski, S. J. Ingleby, O. Sharp, D. P. Burt, P. F. Griffin, J. P. McGilligan, and E. Riis, Optimizing longitudinal spin relaxation in miniaturized optically pumped magnetometers, Phys. Rev. Appl. **22**, 064024 (2024).
[39] B. Cai, C.-P. Hao, Z.-R. Qiu, Q.-Q. Yu, W. Xiao, and D. Sheng, Herriott-cavity-assisted all-optical atomic vector magnetometer, Phys. Rev. A **101**, 053436 (2020).

[40] S.-Q. Liu, Q.-Q. Yu, H. Zhou, and D. Sheng, Sensitive and stable atomic vector magnetometer to detect weak fields using two orthogonal multipass cavities, Phys. Rev. Appl. **19**, 044062 (2023).
[41] S. Li, P. Vachaspati, D. Sheng, N. Dural, and M. V. Romalis, Optical rotation in excess of 100 rad generated by Rb vapor in a multipass cell, Phys. Rev. A **84**, 061403(R) (2011).
[42] S. J. Seltzer, Developments in alkali-metal atomic magnetometry, Ph.D. dissertation, Princeton University, 2008.
[43] B. Lebrun, Y. Jayet, and J.-C. Baboux, Pulsed eddy current signal analysis: Application to the experimental detection and characterization of deep flaws in highly conductive materials, NDT&E Int. **30**, 163 (1997).
[44] B. Boashash, Estimating and interpreting the instantaneous frequency of a signal. i. fundamentals, Proc. IEEE **80**, 520 (1992).
[45] J. Zheng, W. Xiao, S. Li, X. Peng, T. Wu, and H. Guo, Langevin approach to magnetic-field-gradient-induced spin relaxation in a coated cell, Phys. Rev. A **109**, 022803 (2024).
[46] J. J. Moré, The Levenberg-Marquardt algorithm: Implementation and theory, *Numerical Analysis*, edited by G. A. Watson (Springer, Berlin, 1978), p. 105.
[47] H. C. Ohanian, On the approach to electro- and magneto-static equilibrium, Am. J. Phys. **51**, 1020 (1983).
[48] A. E. Barnes, The calculation of instantaneous frequency and instantaneous bandwidth, Geophysics **57**, 1520 (1992).
[49] Y. Li, G. Y. Tian, and A. Simm, Fast analytical modelling for pulsed eddy current evaluation, NDT&E Int. **41**, 477 (2008).
[50] D. J. Griffiths, *Introduction to Electrodynamics* (Cambridge University Press, Cambridge, 2023).
[51] N. Ida and N. Meyendorf, *Handbook of Advanced Nondestructive Evaluation* (Springer, Cham, 2019).
[52] H. Griffiths, Magnetic induction tomography, Meas. Sci. Technol. **12**, 1126 (2001).
[53] L. M. Rushton, T. Pyragius, A. Meraki, L. Elson, and K. Jensen, Unshielded portable optically pumped magnetometer for the remote detection of conductive objects using eddy current measurements, Rev. Sci. Instrum. **93**, 125103 (2022).
[54] C. Deans, L. Marmugi, and F. Renzoni, Active underwater detection with an array of atomic magnetometers, Appl. Opt. **57**, 2346 (2018).
[55] M. Fan, B. Cao, A. I. Sunny, W. Li, G. Tian, and B. Ye, Pulsed eddy current thickness measurement using phase features immune to liftoff effect, NDT&E Int. **86**, 123 (2017).
[56] S. Giguère, B. A. Lepine, and J. M. S. Dubois, Pulsed eddy current technology: Characterizing material loss with gap and lift-off variations, Res. Nondestr. Eval. **13**, 119 (2001).
[57] N. Ulapane and L. Nguyen, Review of pulsed-eddy-current signal feature-extraction methods for conductive ferromagnetic material-thickness quantification, Electronics **8**, 470 (2019).